# Interface optimization and defects suppression via NaF introduction enable efficient flexible Sb2Se3 thin-film solar cells

Mingdong Chen, Muhammad Ishaq, Donglou Ren, Hongli Ma, Zhenghua Su, Ping Fan, David Le Coq, Xianghua Zhang, Guangxing Liang, Shuo Chen

# Interface optimization and defects suppression via NaF introduction enable efficient flexible $Sb_2Se_3$ thin-film solar cells

*Mingdong Chen[a,c], Muhammad Ishaq[a], Donglou Ren[b], Hongli Ma[c], Zhenghua Su[a], Ping Fan[a], David Le Coq[c], Xianghua Zhang[c], Guangxing Liang[a], Shuo Chen[a,*]*

[a]*Shenzhen Key Laboratory of Advanced Thin Films and Applications, Key Laboratory of Optoelectronic Devices and Systems of Ministry of Education and Guangdong Province, College of Physics and Optoelectronic Engineering, Shenzhen University, Shenzhen 518060,Guangdong, China*

[b]*State Key Laboratory of Featured Metal Materials and Life-cycle Safety for Composite Structures, MOE Key Laboratory of New Processing Technology for Nonferrous Metals and Materials, School of Resources, Environment and Materials, Guangxi University, Nanning 530004, Guangxi, China*

[c]*CNRS, ISCR (Institut des Sciences Chimiques de Rennes), UMR 6226, Université de Rennes, Rennes, F-35000, France*

[*]Corresponding author.

*E-mail address*: chensh@szu.edu.cn (S. Chen)

**Keywords:** $Sb_2Se_3$; Flexible solar cells; NaF intermediate layer; Interface optimization; Defects suppression

**Abstract:** $Sb_2Se_3$ with unique one-dimensional (1D) crystal structure exhibits exceptional deformation tolerance, demonstrating great application potential in flexible devices. However, the power conversion efficiency (PCE) of flexible $Sb_2Se_3$ photovoltaic devices is temporarily limited by the complicated intrinsic defects and the undesirable contact interfaces. Herein, a high-quality $Sb_2Se_3$ absorber layer with large crystal grains and benign [hk1] growth orientation can be first prepared on a Mo foil substrate. Then NaF intermediate layer is introduced between Mo and $Sb_2Se_3$, which can further optimize the growth of $Sb_2Se_3$ thin film. Moreover, positive Na ion diffusion enables it to dramatically lower barrier height at the back contact interface and passivate harmful defects at both bulk and heterojunction. As a result, the champion substrate structured Mo-foil/Mo/NaF/$Sb_2Se_3$/CdS/ITO/Ag flexible thin-film solar cell delivers an obviously higher efficiency of 8.03% and a record open-circuit voltage ($V_{OC}$) of 0.492 V. This flexible $Sb_2Se_3$ device also exhibits excellent stability and flexibility to stand large bending radius and multiple bending times, as well as superior weak light photo-response with derived efficiency of 12.60%. This work presents an effective strategy to enhance the flexible $Sb_2Se_3$ device performance and expand its potential photovoltaic applications.

## 1. Introduction

Flexible solar cells and modules can complement the applications in rigid silicon solar cells such as portable equipment, integration in Internet of Things, and building-integration photovoltaics, due to their lightweight, flexibility, and scalability [1–4]. Drawing on dependable thin film preparation technologies, several flexible CdTe, Cu(In,Ga)$Se_2$ (CIGS), organic, and perovskites solar cells have been fabricated and achieved considerable efficiencies (e.g., 20.8% for CIGS [5], 13.6% for CdTe [6], 16.5% for organic [7] and 23.6%

for perovskite [8]). However, the limited availability of component elements (In, Ga, and Te) and their toxic nature (Cd, Pb) may limit large-scale usage of these flexible solar cells [9], and more research over an extended duration is still required to overcome the intrinsic stability challenge of the efficient organic and perovskite solar cells [10,11]. In this regard, thin-film photovoltaic (TFPV) materials composed of environment-friendly, cost-efficient, and intrinsically-stable chemical elements have emerged and drawn tremendous research attention [12].

Among various TFPV alternative candidates, $Sb_2Se_3$ is earth-abundant, less toxic, and highly stable. It also possesses superior optoelectronic properties, including ideal bandgap ($E_g$ of 1.1–1.3 eV), high absorption coefficient (>$10^5$ $cm^{-1}$), decent carrier mobility (~10 $cm^2$ $V^{-1}$ $s^{-1}$), and long carrier lifetime (~60 ns) [13–15]. Moreover, its unique one-dimensional (1D) crystal structure endows it with exceptional deformation tolerance and electrically benign grain boundaries, which makes it more suitable for flexible devices [16–18]. Actually, theoretical calculations confirm that $Sb_2Se_3$'s fracture strain (28% in theory) [16] is significantly larger than that of 3D CdTe (17–18%) and Si (~17%) [19], approaching partially ductile organic polymers. Additionally, the low-temperature (400 °C) synthesis of crystalline $Sb_2Se_3$ facilitates the production of flexible thin-film solar cells on cost-effective metal foil or lightweight polymer substrates [14,19,20].

Rigid $Sb_2Se_3$ solar cells have dragged extensive attention and recently achieved a remarkable efficiency breakthrough (>10 %) [21], while flexible $Sb_2Se_3$ solar cells are less investigated [9,19,22–24], despite their great potential. The highest recorded efficiency of flexible $Sb_2Se_3$ solar cell so far is 8.43% with device configuration of PI/Mo/PbSe/$Sb_2Se_3$/CdS/ZnO/AZO/Ag, which is obviously inferior to that of rigid devices. Currently, the well-researched planar $Sb_2Se_3$ solar cells can be classified into two representative types regarding device structure, i.e., superstrate configuration and substrate configuration [14,21]. With respect to flexible $Sb_2Se_3$ solar cells, for the former scenario, where sunlight enters through the substrate side, the low transmittance of the typical polyimide (PI) substrate in the short wavelength region might result in a significant loss of short-circuit current density ($J_{SC}$) of ~4 mA $cm^{-2}$ [19]. Contrarily, the substrate configuration is necessary for thin-film solar cells on opaque substrates such as flexible metal or plastic foil [9,25]. Actually, the substrate structured solar cells exhibit some important advantages, e.g., modifying the absorber layer efficiently, designing the interface independently, and presenting more possibilities in tandem or flexible solar cells [26]. The first report of substrate structured flexible $Sb_2Se_3$ thin-film solar cell is about $Sb_2Se_3$ absorber layer deposited on flexible molybdenum (Mo) foil via vapor transport deposition (VTD) accompanied by two-step treatment, achieving an efficiency of 5.35% with $J_{SC}$ of 28.22 mA $cm^{-2}$, $V_{OC}$ of 0.370 V and fill factor (FF) of 51.90% [9]. The severe $V_{OC}$ deficit (defined as $E_g/q-V_{OC}$) can be mainly attributed to the existence of complicated deep defects at bulk and interface. Our group has made great efforts to overcome this core challenge and achieved considerable progress [13,20,27]. Especially, an effective absorber layer growth engineering incorporating VTD and post-selenization was developed to prepare $Sb_2Se_3$ with large compact crystal grains and benign [hk1] growth orientation [27]. A minimum $V_{OC}$ deficit has been obtained, which could provide essential guidance for the development of flexible solar cells based on $Sb_2Se_3$. In parallel, the low FF of flexible substrate structured $Sb_2Se_3$ device might result from the unsatisfactory contact at the $Sb_2Se_3$/Mo interface, where Schottky contacts are easily formed [28–30]. The high contact barrier strongly influences photo-generated holes' extraction and transport, resulting in serious carrier recombination at the buried bottom interface [31–33]. To cope with this issue, Mai et al. demonstrated that the additional Mo selenization process (e.g., at 620 °C for 20 min) with the formation of $MoSe_2$ intermediate nanolayer (~20 nm) could optimize the back contact interface and improve the carrier collection efficiency, leading to a

high FF of 58.15% in planar substrate structured $Sb_2Se_3$ solar cell and even 70.3% in core-shell structured $Sb_2Se_3$ nanorod array solar cell [28,34]. However, for most flexible substrates, such high selenization temperature is a nonnegligible challenge, even with great heat tolerance, the diffusion of impurity components from the substrate to the absorber layer might result in complex defects [25]. Moreover, metal foils normally have a high surface roughness that might penetrate cells, causing current leakage. Therefore, to further improve the performance of substrate-structured $Sb_2Se_3$ flexible devices, further efforts should be made to address the detrimental defects in the bulk layer and the poor quality at the back interface.

In this work, under the guidance of our previously valuable experience, an optimized VTD and post-selenization technique were implemented to prepare high-quality $Sb_2Se_3$ thin film on flexible Mo foils. The substrate-structured flexible device exhibited an efficiency of 5.90% with similar $V_{OC}$ and $J_{SC}$ to the champion rigid device, however, a substantially lower FF of 49.63%. Afterwards, sodium fluoride (NaF) was introduced as an interface layer to improve the back contact quality. Besides, thanks to the Na diffusion into the $Sb_2Se_3$ absorber layer, facilitating simultaneous passivation of defects at bulk and heterojunction interface. As a result, the efficiency of the NaF-treated cell rose to a competitive value of 8.03%, accompanied by obviously increased $V_{OC}$ and FF of 0.492 V and 62.30%, respectively. Additionally, these flexible $Sb_2Se_3$ devices demonstrated excellent flexibility, being able to withstand large bending radius ($R$>2 mm) and bending cycles (>1000 times) without noticeable PCE degradation.

## 2. Experimental

### *2.1. Device fabrication*

Flexible $Sb_2Se_3$ solar cells were fabricated as Mo-foil/Mo/$Sb_2Se_3$/CdS/ITO/Ag device structures. Mo foil (40 × 40 × 0.03 $mm^3$) substrates were first subjected to a sequential cleaning process involving detergent, ethanol, and deionized water in an ultrasonic bath for 10 min. Mo as a back contact layer was then sputtered on Mo foils using direct current (DC) magnetron sputtering based on a Mo target of 99.99% purity. A double-pressure sputtering process was employed to deposit Mo with a total thickness of approximately 0.7 μm, consisting of an initial deposition at 1.2 Pa for 15 min to enhance adhesion followed by a subsequent deposition at 0.3 Pa for 30 min to ensure compactness. Next, an NaF intermediate layer with a thickness of 5, 10, or 20 nm was deposited on the bi-layer of Mo by a thermal evaporator with a base pressure lower than $8 \times 10^{-4}$ Pa. In detail, the 0.2 g of NaF powder (99.99% purity, Aladdin) was placed in a Mo boat, and during the deposition, the substrate did not require additional heating. Subsequently, $Sb_2Se_3$ light absorbers were deposited onto the Mo-coated Mo foil substrates via VTD method, following an optimized procedure as previously reported [27]. $Sb_2Se_3$ absorbers were then subjected to an additional post-selenization heat treatment in a vacuum tubular furnace, and the temperatures were varied from 400, 420 to 440 °C. A CdS buffer layer, approximately 70 nm thick, was deposited on the surface of $Sb_2Se_3$ using chemical bath deposition (CBD) method. The resulting layer was then rinsed with deionized water and dried in an oven. Indium tin oxide (ITO) window layer was subsequently deposited via radio-frequency (RF) sputtering at a power of 100 W, pressure of 0.35 Pa, and flow rates of 30 sccm for argon and 5 sccm for oxygen gas. Finally, Ag electrodes were deposited onto the ITO surface via thermal evaporation through a mask and defined by a knife scribe to form an isolated area of 0.14 $cm^2$. Overall, a schematic diagram of the device fabrication process is illustrated in Fig. S1.

### *2.2. Characterizations*

The crystallization information of $Sb_2Se_3$ was characterized via X-ray diffraction (XRD, Ultima-iv) with Cu $K_\alpha$ radiation under operational conditions of 40 kV and 40 mA. The surface and cross-sectional morphologies of $Sb_2Se_3$ thin films and devices were observed through scanning electron microscopy (SEM, Zeiss SUPRA 55). A Keithley 2400 multi-meter was used to measure the current density voltage (*J-V*) characteristics under simulated AM 1.5G sunlight and the intensity was calibrated to 100 mW $cm^{-2}$. The external quantum efficiency (EQE) spectra were tested using a Zolix SCS101 system equipped with a Keithley 2400 source meter. The ohmic contact properties of Mo/$Sb_2Se_3$ back contact were tested by the multi-meter (Keithley, 2400 Series). The electrochemical impedance spectroscopy (EIS) of devices was characterized by the CHI600E electrochemical workstation. The temperature-dependent dark *J-V* (*J-V-T*) measurement was performed using a Lakeshore 325 temperature controller and Keithley 4200A-SCS system. Capacitance-voltage (*C-V*) measurements were conducted under dark conditions at room temperature, with a frequency of 10 kHz and a sweeping DC bias voltage ranging from −1 to 0.3 V, accompanied by an attached AC amplitude of 30 mV. Drive-level capacitance profiling (DLCP) measurements were performed at DC bias voltage from −0.2 to 0.2 V and modulated with AC amplitude from 0.02 to 0.14 V. Capacitance-frequency (*C-f*) measurements were performed over a frequency range spanning from 1 kHz to 10 MHz. All the temperature-dependent measurements were implemented using a cryogenic system (Janis VPF-100) cooled by liquid nitrogen. For the purpose of weak light performance testing, a monochromatic light source with an adjustable power output of 80 mW and a wavelength of 635 nm (MRL-Ⅲ-635L) was utilized in conjunction with a source meter (Keithley 2400). The intensity of the light was calibrated using a silicon photo-detector (Newport 818-UV).

## 3. Results and discussion

In our previous work, we have developed an effective technique for growing high-quality $Sb_2Se_3$ thin films on a rigid soda-lime glass (SLG) substrate, which involves pre-VTD and post-selenization heat treatment [27]. Herein, the $Sb_2Se_3$ absorber layer on Mo foils was prepared by following a similar procedure under optimal conditions. The scanning electron microscopy (SEM) characterization was first conducted to investigate the surface morphology and structural characteristics of the $Sb_2Se_3$ thin films deposited on glass (Fig. S2a, Supporting Information) and flexible Mo-foil substrate (Fig. 1a), and labeled as Glass and Mo-foil, respectively. Quite similar $Sb_2Se_3$ thin films with large compact crystal grains can be obtained, and the average grain size is approximately 1.6 μm (Fig. S3). Importantly, the absence of cracks on Mo-foil $Sb_2Se_3$ thin films after bending at a 2 mm radius indicated the high flexibility of $Sb_2Se_3$. X-ray diffraction (XRD) patterns of Glass and Mo-foil $Sb_2Se_3$ thin films are displayed in Fig. 1(b). The acquired samples show distinct peaks that are well-concordant with the orthorhombic phase of $Sb_2Se_3$ on the JCPDS standard card (No. 15-0861) and free of impurities or secondary products. In particular, both $Sb_2Se_3$ thin films exhibit (211), (221), (301), and (002) sharp diffraction peaks, indicating strong [hk1] preferential growth orientation. Furthermore, the full width at half maximum (FWHM) of the representative (211) and (221) peaks were nearly overlapped (Fig. 1c), echoing its SEM analysis. The flexible $Sb_2Se_3$ thin-film solar cells with substrate configuration were fabricated. The cross-sectional SEM images of the flexible Mo-foil/Mo/$Sb_2Se_3$/CdS/ITO and the Glass/Mo/$Sb_2Se_3$/CdS/ITO solar cells are shown in Fig. 1(d) and Fig. S2(b), respectively. The layers of the device are readily discernible and distinguishable. For the Mo-foil $Sb_2Se_3$ device, the thicknesses of Mo, $Sb_2Se_3$, CdS, and ITO layers were about 700 nm, 1.2 μm, 70 nm, and 400 nm, respectively (Table S1, Supporting Information). Among them, $Sb_2Se_3$ layer was composed of large, densely packed crystal grains that exhibit nearly vertical orientation throughout the entire light absorber layer. Such observations were found to be in excellent agreement with the

corresponding XRD results, and the thin film with dominant [hk1]-oriented grains exhibited fewer dangling bonds at grain boundaries, which could potentially enhance carrier transport and mitigate carrier recombination [17]. Actually, it is closely related to the intrinsic 1D crystal structure of $Sb_2Se_3$ (inset in Fig. 1f). The $[Sb_4Se_6]_n$ ribbons are covalently bonded by Sb-Se along the *c*-axis, while they are connected through weak van der Waals (vdW) forces in the *a*-axis and *b*-axis directions [35]. Thus, the as-prepared $Sb_2Se_3$ thin film with [hk1] orientation can tolerate large deformations, providing fundamental support for its highly flexible thin-film devices. Moreover, for thin-film solar cell, based on the basic laws of material mechanics in a multi-layered system, the strain can be calculated using the neutral axis (NA) concept (Fig. 1e) [19,36]. The location of NA is influenced by the Young modulus, Poisson ratio, and layer thickness (detailed calculation process is provided in Supplementary note 1). Based on the computed results, it can be inferred that the NA will be in close proximity to the $Sb_2Se_3$ layer when the Mo-foil substrate is about 30 μm. The ITO layer, inherently rigid and brittle, is the farthest from the NA and suffers the largest strain. Therefore, if the strain applied to the ITO layer exceeds its critical fracture strain of approximately 1% [37], irreversible damage will occur, significantly impacting the performance of flexible $Sb_2Se_3$ solar cells. We quantitatively calculated the strain of the whole device, $Sb_2Se_3$, CdS and ITO layers as a function of curvature radii ($R$), as shown in Fig. 1(f). When the critical strain of ITO is 1%, the critical $R$ is 1.45 mm, and the strain of the devices and the $Sb_2Se_3$ absorber layer at this time is less than 1%. It reveals that 1% strain is located in the elastic strain region, wherein, the strain of our devices can fully recover after bending under practical working conditions.

The statistical distributions of key performance parameters including the $V_{OC}$, $J_{SC}$, FF and the efficiencies are shown in Fig. 2(a–d), to evaluate the influence of post-selenization temperatures on the flexible $Sb_2Se_3$ thin-film solar cell performance, as well as a comparison to that of the isotypic rigid (Glass-based) device. The four series of devices, each comprising twenty-five sub-cells processed synchronously, exhibited acceptable reproducibility. It is obvious that an appropriate post-selenization temperature (i.e., 420 °C) helps to enhance the flexible device performance, and all parameters start to deteriorate under lower or higher temperature, which is consistent with the variation of rigid $Sb_2Se_3$ counterparts with an optimal post-selenization temperature of 420 °C. The current density-voltage (*J-V*) curves of the champion flexible Mo-foil based device and the referenced Glass based $Sb_2Se_3$ solar cells are presented in Fig. 2(e). It can be obtained that the champion efficiency of Mo-foil flexible $Sb_2Se_3$ device is 5.90% with a $V_{OC}$, $J_{SC}$, and FF of 0.479 V, 24.81 mA $cm^{-2}$ and 49.63%, respectively. It already out-performs the previously reported VTD-processed substrate structured $Sb_2Se_3$ flexible solar cell (PCE of 5.35%). However, it is really inferior to the rigid Glass device, which exhibits 7.34% PCE with a $V_{OC}$ of 0.513 V, a $J_{SC}$ of 24.20 mA $cm^{-2}$ and FF of 59.11%. The detailed device performance parameters of each category are summarized in Table 1. Distinctly, $V_{OC}$ and FF deficits account for the efficiency loss of flexible devices in comparison with that of the rigid device. The corresponding EQE and integrated $J_{SC}$ for both devices are portrayed in Fig. 2(f). The integrated current densities of Mo-foil and Glass devices are 24.51 and 23.96 mA $cm^{-2}$, respectively, which closely correspond to the $J_{SC}$ values obtained from *J-V* measurement results. In the wavelength range of 350 to 900 nm, the nearly overlapped EQE spectra demonstrate that the flexible $Sb_2Se_3$ device can realize effective carrier collection and transport. Furthermore, the tail states can be quantified by means of Urbach energy ($E_u$), which was calculated from the EQE in the long wavelength edge [38]. The estimated $E_u$ values are approximately 29–33 meV (Fig. 2g), which is comparable to that of previously reported high-efficiency antimony chalcogenide solar cells, owing to the alleviative defects at grain boundaries under [hk1] orientation [13,39,40]. In contrast, a slightly larger $E_u$ for the flexible device can be ascribed to the electrostatic

potential fluctuations, typically derived from the deep defects at the interface and/or within the bulk film, ultimately limiting its $V_{OC}$ [41]. In order to extract the key diode parameters of the solar cells, a single exponential diode equation is employed to compare and analyze the dark *J-V* curves of representative Glass and Mo-foil $Sb_2Se_3$ devices [27].

$$J = J_0 \exp\left[\left(\frac{q}{AkT}\right)(V - JR_s)\right] + G_{sh}V - J_L \quad (1)$$

where $G_{sh}$, $R_s$, $A$, and $J_0$ represent the shunt conductance, series resistance, ideality factor, and reverse saturation current, respectively, $k$ is the Boltzmann constant, and $q$ is the elementary charge on the electron. The fitting results are illustrated in Fig. 2(h). The $R_s$ values are linearly fitted as 2.28 and 5.51 Ω cm$^2$ for Glass and Mo-foil $Sb_2Se_3$ devices. The obtained $A$ values of 1.93 and 2.18 suggest the coexistence of interface and space charge region (SCR) recombination in both devices. In addition, the flexible device exhibits no significant increase in SCR recombination caused by the trap levels in the depletion region. To further investigate the defect states, a typical model of space charge-limited current (SCLC) was employed. The logarithmic *J-V* characteristic curves in Fig. 2(i) can be divided into three regions: ohmic, trap-filled limit (TFL), and trap-free Child [20]. The onset voltages in the TFL region ($V_{TFL}$) were determined to be 0.17 and 0.24 V for Glass and Mo-foil $Sb_2Se_3$ devices, respectively. The calculation of trap state density ($N_{trap}$) was subsequently performed [42].

$$N_{trap} = \frac{2\varepsilon_0\varepsilon_r V_{TFL}}{L^2 q} \quad (2)$$

where $L$ is the thickness of $Sb_2Se_3$ thin film, $\varepsilon_0$ is the vacuum permittivity, and $\varepsilon_r$ is the relative permittivity (i.e., 15.1 for $Sb_2Se_3$). The relatively higher $N_{trap}$ value ($1.77 \times 10^{14}$ cm$^{-3}$) for Mo-foil $Sb_2Se_3$ suggests it possesses more trap sites and defect centers. Overall, the $E_u$, $R_s$, $A$, and $N_{trap}$ of the flexible $Sb_2Se_3$ devices deteriorate slightly, resulting in a decrease in $V_{OC}$, FF, and PCE. Thus, further engineering efforts are necessary to enhance the efficiency of flexible $Sb_2Se_3$ solar cells.

Introducing an appropriate intermediate layer between the back electrode and absorber layer is a highly effective strategy for addressing the poor quality of the back interface [43,44]. In this regard, NaF has been extensively employed as back interface layer in well-researched CIGS, kesterite, and perovskite solar cells, and demonstrated positive effects in promoting crystal growth, optimizing interface contact, and passivating detrimental defects [45–47]. To start, we adjusted the thickness of the NaF interface layer and found the best device performance occurred at NaF thickness of around 10 nm (Fig. S4). Meanwhile, $Sb_2Se_3$ thin film with NaF can still maintain the ideal microstructure characteristics (Fig. S5). *J-V* curves of the champion flexible Mo-foil $Sb_2Se_3$ devices without NaF (denoted as W/O NaF) and with additional NaF (denoted as With NaF) are shown in Fig. 3(a). The NaF Mo-foil $Sb_2Se_3$ device demonstrates a champion efficiency of 8.03% with a $V_{OC}$ of 0.492 V, a $J_{SC}$ of 26.21 mA cm$^{-2}$, and an FF of 62.30%, which are much higher than those of the W/O NaF counterpart. Table 2 and Fig. S6 present another comparison with state-of-the-art flexible $Sb_2Se_3$ solar cells that have been reported. The PCE of 8.03% is slightly inferior to the highest value of 8.43% belonging to Mo/PbSe/$Sb_2Se_3$/CdS/ZnO/AZO/Ag thin-film solar cell with imperfect PbSe as back-contact transition layer. Furthermore, the maximum $V_{OC}$ of 0.492 V is the highest value among all flexible $Sb_2Se_3$ solar cells (Fig. S6a). Generally, the low FF in the Mo-based chalcogenide solar cells is associated with high dark series resistance ($R_{S,D}$). To further elucidate this issue of the FF and efficiency improvement with introducing NaF layer, the ohmic contact between Mo/$Sb_2Se_3$ and the series resistance ($R_S$) was initially investigated. The *I-V* curves in Fig. S7(a) were obtained from the Glass/Mo/$Sb_2Se_3$/Ag device construction. All linear *I-V* curves suggest the formation of an ohmic contact at the Mo/$Sb_2Se_3$ interface.

The resistance curves and slopes of all samples are shown in Fig. S7(b). The slopes for With NaF and W/O NaF were measured at 0.844 and 0.656 S, with corresponding resistances of 1.18 and 1.52 Ω, respectively. The results illustrate that incorporating an NaF layer with appropriate thickness improves the ohmic behavior at the back contact, promoting efficient transport of photogenerated holes. We then scrutinized the temperature-dependent current density voltage (*J-V-T*) evolutions in the dark condition covering temperature range from 200 to 300 K. A standard diode model was utilized, and the $R_{S,D}$ values were obtained from the plot of d$V$/d$J$ versus 1/($J-G_D V$) following equation [48].

$$\mathrm{d}V/\mathrm{d}J = R_{S,D} + AkT/q(J - G_D V) \quad (3)$$

where $A$, $k$ and $G_D$ are the diode ideality factor, Boltzmann constant, and the dark shunt conductance, respectively. The dark series resistance $R_{S,D}$ was selected to prevent light-derived alterations in the series resistance that might occur under illumination. The $R_{S,D}$ can be obtained through the $y$-intercept, and a diverging $R_{S,D}$ toward lower temperature can be observed. As shown in Fig. 3(b), with temperature decreasing from 300 to 200 K, $R_{S,D}$ of the W/O NaF device increased by nearly two orders of magnitude, whereas only an increase of $R_{S,D}$ of 3.5 times for the With NaF device. A blocking contact barrier may be the cause of the high series resistance observed in the W/O NaF device at low temperatures, in addition to background resistance ($R_0$). This barrier is reasonably expected to occur at the interface of Mo and $Sb_2Se_3$, thereby suppressing the transport of majority carriers (holes). The back contact junction was modeled as Schottky diode to describe the flexible solar cell (inset in Fig. 3b). The corresponding circuit model comprises a primary solar cell diode ($D_{SC}$), and a series resistance $R_{S,D}$ that encompasses both background series resistance ($R_0$) and back contact diode ($D_{BC}$) [49]. When the solar cell was forward-biased, the $D_{BC}$ experiences reverse bias and its conduction is limited by $J_0$, which decreases rapidly at lower temperatures, leading to an increase in $R_{S,D}$ value. The total temperature-dependence of $R_{S,D}$ in the solar cell can be described by the following equation [48]:

$$R_{S,D} = R_0 + \frac{k}{qA^*T} \times \exp\left(\frac{\Phi_B}{kT}\right) \quad (4)$$

where $A^*$ is the effective Richardson constant, and $\Phi_B$ is the blocking contact barrier height, as illustrated in Fig. 3(c). $R_0$ is the background series resistance from various functional layers, which is assumed to be negligible at lower temperature ($T$<300 K) [48]. The barrier height $\Phi_B$ extracted by fitting the corresponding linear region of ln($R_{S,D}T$) versus 1/$T$ plots. The obtained $\Phi_B$ values of the W/O NaF and With NaF devices are 241 and 55 meV, respectively. The lower $\Phi_B$ value is considered to be a better Ohmic contact, indicating an enhanced carrier transport and collection at the buried bottom interface, consistent with its lower $R_S$ and higher FF [44]. Additionally, the cross-over behavior between the light and dark *J-V* points to the existence of a blocking back contact (Fig. 3a) [44,48]. These cross-over points occur at a higher current with additional NaF layer, which corresponds to decreasing $\Phi_B$ in device. Furthermore, dark *J-V-T* measurements was also utilized to clarify the recombination mechanisms in flexible $Sb_2Se_3$ solar cells, especially under this interface engineering. The diode ideality factor $A$ of the With NaF device is calculated to be 1.62 according to eq. (3), which demonstrates a significant decrease compared to that of the W/O NaF device (as shown in Table 3), indicating that the introduction of the NaF intermediate layer can improve the quality of the $Sb_2Se_3$/CdS interface and reduce the interface recombination, and SCR recombination caused by trap levels in the depletion region is significantly diminished. A predominant recombination pathway can be determined by plotting $A$ln($J_0$) against 1/$kT$, utilizing the following equation [50]:

$$A\ln(J_0) = A\ln(J_{00}) - \frac{E_a}{kT} \quad (5)$$

where $J_{00}$ is a pre-factor dependent on recombination paths, $E_a$ is recombination activation energy, which can be obtained from the slope of $A\ln(J_0)$ against $1/kT$ plots. In principle, the dominant recombination mechanism can be evaluated by comparing the $E_a$ with the bandgap ($E_g$) of the $Sb_2Se_3$ absorber layer. As illustrated in Fig. 3(d), the estimated $E_a$ of W/O NaF device is 0.95 eV, much smaller than the $E_g$ (1.30 eV determined from EQE data) of the as-prepared $Sb_2Se_3$, signifying a dominant and severe defect-assisted interface recombination. In contrast, an enlarged $E_a$ value of 1.19 eV belonging to With NaF device is much closer to its $E_g$ value, which authenticates the suppression of overall recombination loss through mitigatory bulk or SCR recombination in a dominant manner, leading to much superior device $V_{OC}$ and PCE. The distribution of the elements was investigated using time-of-flight secondary ion mass spectrometry (ToF-SIMS), as shown in Fig. 3(e and f). Except for reasonable Sb and Se signals that existed in the $Sb_2Se_3$ absorber layer, Na ions can also be observed, especially with relatively higher SIMS intensity at the bottom and top interface. It is likely to occur under post-selenization heat treatment, and Na ion tends to diffuse across the $[Sb_4Se_6]_n$ ribbons due to the radius of $Na^+$ (0.102 nm) being smaller than the gap between the ribbons (~0.35 nm).

To further examine the working mechanism behind this significant photovoltaic performance improvement, capacitance-voltage (*C-V*) and DLCP measurements have been implemented. The higher $V_{OC}$ is also explained by the improvement in the built-in voltage ($V_{bi}$) from 0.593 to 0.648 V after NaF introduction, as indicated in the $1/C^2$-$V$ curves (Fig. 4a). It demonstrates an increase in charge accumulation at the heterojunction interface and a decrease in trap states. The discrepancy between *C-V* and DLCP profiling at zero bias is normally related to the presence of interface defects ($N_i$) [27]. The discrepancy between $N_{C\text{-}V}$ and $N_{DLCP}$ of the W/O NaF flexible $Sb_2Se_3$ device was observed to be larger than that of the With NaF device, As illustrated in Fig. 4(b). The estimated $N_i$ values were $3.63 \times 10^{15}$ and $1.45 \times 10^{15}$ $cm^{-3}$ (at $v$ = 0 V), respectively, signifying an improved $Sb_2Se_3$/CdS heterojunction quality with NaF treatment. It might be assigned to the smoother surface and Na ions diffusion in the $Sb_2Se_3$ absorber (Fig. S5a and Fig. 3e). In addition, the With NaF device exhibited a slightly larger depletion width ($W_d$) (247 nm), which is undoubtedly favorable for the separation and extraction of carrier, thereby contributing to a significantly enhanced photovoltaic performance. The various heterojunctions or interface-associated parameters are summarized in Table 3. It is worth noting that effective back contact interface engineering can modify the junction quality, interface quality, and the charges recombination mechanism. EIS analysis was also conducted to examine the charge recombination and charge transfer characteristics of the solar cells. As shown in Fig. S8, a higher recombination resistance in With NaF confines the charge recombination at $Sb_2Se_3$/CdS and back contact interface, resulting in improved $V_{OC}$, $J_{SC}$, and FF. Subsequently, admittance spectroscopy (AS) was performed to investigate the bulk defect characters. Fig. 4(c and d) show capacitance-frequency (*C-f*) spectra obtained under dark conditions at various temperatures from 300 to 110 K with an increment of −10 K for the champion W/O and With NaF flexible $Sb_2Se_3$ devices, respectively. In general, the high frequency capacitance reflects free carrier response while the low frequency capacitance reflects both free carrier and deep-level defect responses [51]. Thus, it can be deduced that the With NaF device possessed lower trap densities within the absorber layer. Moreover, only one capacitance step (i.e., the maxima $f_{max}$ of the derivative $-\mathrm{d}C/\mathrm{d}\ln f$ in both devices can be differentiated with varying frequencies, which corresponds to a defect level. The inflection frequencies ($\omega_0 = 2\pi f_{max}$) as a function of temperature can be determined by plotting the $-\mathrm{d}C/\mathrm{d}\ln f$ curves (not shown here). The Arrhenius plots of $\ln(\omega_0/T^2)$ versus $1000/T$ at the inflection points in both admittance spectra are shown in Fig.

4(e and f). The defect activation energy ($E_a$) can be determined by fitting the Arrhenius plot yielded according to the following equation [52]:

$$\omega_0 = 2\pi v_0 T^2 \exp\left(\frac{-E_a}{kT}\right) \quad (6)$$

where $v_0$ is the attempt-to-escape frequency, $\omega_0$ is the inflection point frequency of each AS curve, and $E_a$ is the defect activation energy that reflects the depth of a defect's energy level compared to the corresponding band edge. As shown in Fig. 4(e), the synchronous temperature-dependent variation as well as the absence of activation energies in the low-temperature region for both the devices suggest that the introduction of NaF would not bring any additional defects, neither at bulk nor at the surface/interface. The derived $E_a$ values were 462 and 426 meV for the W/O NaF and With NaF devices, respectively, such a small energy gap ($\Delta E_a$ = 36 meV) confirms the existence of identical defect types in these two devices. Based on the first-principle theoretical basis and experimental findings reported in literature, the dominant defects with corresponding $E_a$ values in this scenario can be assigned to $Sb_{Se}$ antisite defects [20]. Moreover, it can hypothesize that the diffused $Na^+$ is most likely inert, which would not modify the band structure and defect physics of $Sb_2Se_3$. The distribution of defects was then Gaussian fitted using the Kimerling model according to the following equations [53]:

$$E(\omega) = kT\ln\left(\frac{2\pi v_0 T^2}{\omega}\right) \quad (7)$$

$$N_t(E(\omega)) = -\frac{V_d \,\mathrm{d}C\ \omega}{q\omega \mathrm{d}\omega kT} \quad (8)$$

where $N_t(E(\omega))$ is the defect density, $V_d$ is the built-in voltage of the heterojunction, and $\omega$ is the angular frequency. The integrated defect densities of the W/O NaF and With NaF flexible $Sb_2Se_3$ devices are $7.56 \times 10^{16}$ and $3.14 \times 10^{16}$ $cm^{-3}$, respectively, as illustrated in Fig. 4(f). As a result, after NaF introduction, the smaller $E_a$ value indicates a quicker hole emission rate, which is less likely to behave as recombination centers, accompanied by a significant decrease of defect density by nearly half, which is positive to alleviate the $V_{OC}$ deficit since it being proportional to $A\ln N$ (where $A$ is the ideal factor, and $N$ signifies the density of the recombination center), thereby improving the device performance. Overall, the results of *C-V*, DLCP and AS tests indicate that the interface defect density and bulk defect density of With NaF devices are significantly lower compared to those of W/O NaF devices. The SIMS study also confirmed the successful incorporation of Na ions into the absorber layer and the heterojunction interface, enhancing the P-type doping of the $Sb_2Se_3$ absorber layer and $Sb_2Se_3$/CdS heterojunction. Thus, the NaF interface layer not only effectively improves the back contact but also optimizes the quality of the heterojunction and the absorber layer, boosting the FF, $V_{OC}$, and PCE of the flexible $Sb_2Se_3$ device.

Deformability is an important criterion for flexible devices to be applied on practical occasions. To investigate the flexible properties of the champion With NaF flexible $Sb_2Se_3$ thin-film solar cell, the device performance was recorded after bending at a different curvature radius of 5, 4, 3, 2, 1.5, and 1 mm (Fig. 5a). The flexible $Sb_2Se_3$ solar cells can withstand a bending radius of $R$>2 mm and return to their original state. The normalized degradation of PCE in solar cells under various bending radii was measured and presented in Fig. 5(b), and the detailed performance parameters are provided in Fig. S9(a) and Table S2 (Supporting Information). When the bending radius exceeds 2 mm, it is observed that the $V_{OC}$ and FF of the device remain largely unaltered, while the $J_{SC}$ decreases slightly, from 25.70 to 24.76 mA $cm^{-2}$. This minor reduction in $J_{SC}$ can be primarily attributed to the diminished

light-accepting area of the device, while the structural integrity of each functional layer remains uncompromised. As a result, the PCE exhibited only a relatively 4.7% reduction of the initial value. However, at bending radii less than 2 mm, a noticeable decline in the device's photovoltaic parameter was observed, with a particularly rapid decrease in the FF contributing significantly to the reduction in PCE, which is consistent with our calculated results presented in Fig. 1(f). This bending level is close to the limited bend radius of curvature of ITO (1.5 mm), which may cause the ITO layer to break, thereby degrading the device performance. Furthermore, the photovoltaic parameters ($V_{OC}$, FF, and $J_{SC}$) of the device exhibit a slight decrease with increasing bending cycles (as illustrated in Fig. 5c, the maximum radius of bending is 3 mm), indicating that each functional layer is gradually destroyed by stretching stress. The corresponding *J-V* curves and the detailed performance parameters of the devices before and after bending treatments are provided in Fig. S9(b) and Table S3. Accordingly, an acceptable 6.5% efficiency reduction can be observed, demonstrating the high flexibility and mechanical robustness of our flexible Mo-foil $Sb_2Se_3$ solar cells. Furthermore, replacing the rigid and fragile ITO electrodes with flexible transparent conductive electrodes or conductive carbon nanomaterials might further increase the flexibility of $Sb_2Se_3$ solar cells. Working at indoor or weak light scenarios is an important advantage for flexible devices. The performances of flexible $Sb_2Se_3$ solar cells bending at a 3 mm R were tested using LED light illumination, and the light intensity was calibrated with an illuminometer. Device *J-V* curves under LED light intensities ($I$) of 0.16–3.37 mW cm$^{-2}$ are shown in Fig. 5(d). All the curves with obvious rectification effects indicated an excellent response to weak light. The light intensity dependent photovoltaic parameters evolutions are shown in Fig. 5(e) and Fig. S10, wherein, an interesting 12.60% efficiency can be obtained at 2.83 mW cm$^{-2}$, with a $V_{OC}$ of 0.431 V, $J_{SC}$ of 1.70 mA cm$^{-2}$, and FF of 50.04%. Moreover, the $J_{SC}$ values exhibit a remarkable power-law relationship with light intensities, as indicated by $J_{SC} \propto I^{\alpha}$ (Fig. 5(e) illustration). A power value $\alpha$ of 0.992 is quite close to 1, indicating that the $Sb_2Se_3$ solar cell possesses excellent photo-response for weak light, and the space-charge limited photocurrent is negligible [54]. By contrast, $V_{OC}$ decreases logarithmically as light intensity decreases, and can be accurately described by the relation $V_{OC} = 0.391 + 0.039 \times \ln(I)$, which is in good agreement with the relation $V_{OC} = V_{OC,\,ref} + (Ak_BT/q) \times \ln(I)$, where $V_{OC,\,ref}$ is the open-circuit voltage at 5.36 mW cm$^{-2}$, $A$ is the ideality factor of the junction diode, $q$ is the electron charge, $k_B$ is Boltzmann's constant and $T$ is the temperature [55]. The ideality factor $A$ derived from $V_{OC}$ fitting is 1.51 (the fitting result of dark *J-V* curve is 1.62), indicating reduced SRH recombination under low-intensity light radiation, strengthening its great potential in indoor or weak light photovoltaic applications.

## 4. Conclusions

In summary, high-quality $Sb_2Se_3$ light absorbers were successfully deposited on flexible Mo foils via vapor transport deposition followed by post-selenization. The efficiency of the flexible Mo-foil/Mo/$Sb_2Se_3$/CdS/ITO/Ag solar cell was 5.90%, but inferior to that of Glass based rigid counterpart. Then, a thin NaF intermediate layer was thermally inserted between Mo and $Sb_2Se_3$, which has been found to significantly improve the back contact quality and enhance the carrier transport capability. Moreover, the Na ions diffusion into the $Sb_2Se_3$ absorber layer could positively passivate the defects at bulk and heterojunction interface, and therefore suppress defect-assisted recombination. Consequently, the NaF-assisted device demonstrated obviously increased $V_{OC}$ to 0.492 V, and FF to 62.30%, yielding a stimulating efficiency of 8.03%. This flexible device demonstrated exceptional deformability, maintaining 95.3% of its initial efficiency bending at the curvature radius of 2 mm, and 93.5% after 1000 bending cycles. In addition, a remarkable weak light photo-response with 12.60% efficiency at 2.83 mW cm$^{-2}$ can be obtained. This study presents a straightforward interface

treatment strategy to effectively improve flexible $Sb_2Se_3$ photovoltaic device performance, broadening its flexible and/or indoor application scenarios.

**Declaration of competing interest**

The authors declare that they have no known competing financial interests or personal relationships that could have appeared to influence the work reported in this paper.

**Acknowledgments**

This work was supported by the National Natural Science Foundation of China (Nos. 62104156, 62074102), the Guangdong Basic and Applied Basic Research Foundation (2023A1515011256, 2022A1515010979) China, Science and Technology plan project of Shenzhen (20220808165025003, 20200812000347001) China. This project was also supported by the open foundation of Guangxi Key Laboratory of Processing for Non-ferrous Metals and Featured Materials, State Key Laboratory of Featured Metal Materials and Life-cycle Safety for Composite Structures, Guangxi University (Grant No. 2022GXYSOF13).

**Appendix A. Supplementary data**

Supplementary data to this article are provided.

**References**

[1] Y. Hu, T. Niu, Y. Liu, Y. Zhou, Y. Xia, C. Ran, Z. Wu, L. Song, P. Müller-Buschbaum, Y. Chen, W. Huang, ACS Energy Lett. 6 (2021) 2917-2943.

[2] J. Wang, K. Li, J. Tang, C. Chen, Sol. RRL 7 (2023) 2300436.

[3] L. Li, S. Zhang, Z. Yang, E.E.S. Berthold, W. Chen, J. Energy Chem. 27 (2018) 673-689.

[4] C. Xie, C. Xiao, J. Fang, C. Zhao, W. Li, Nano Energy 107 (2023) 108153.

[5] R. Carron, S. Nishiwaki, T. Feurer, R. Hertwig, E. Avancini, J. Löckinger, S.-C. Yang, S. Buecheler, A.N. Tiwari, Adv. Energy Mater. 9 (2019) 1900408.

[6] J. Ramanujam, D.M. Bishop, T.K. Todorov, O. Gunawan, J. Rath, R. Nekovei, E. Artegiani, A. Romeo, Prog. Mater. Sci. 110 (2020) 100619.

[7] W. Song, K. Yu, J. Ge, L. Xie, R. Zhou, R. Peng, X. Zhang, M. Yang, Z. Wei, Z. Ge, Matter 5 (2022) 1877-1889.

[8] M. Li, J. Zhou, L. Tan, H. Li, Y. Liu, C. Jiang, Y. Ye, L. Ding, W. Tress, C. Yi, The Innovation 3 (2022) 100310.

[9] C. Wang, S. Lu, S. Li, S. Wang, X. Lin, J. Zhang, R. Kondrotas, K. Li, C. Chen, J. Tang, Nano Energy 71 (2020) 104577.

[10] S. Savagatrup, A.D. Printz, T.F. O'Connor, A.V. Zaretski, D. Rodriquez, E.J. Sawyer, K.M. Rajan, R.I. Acosta, S.E. Root, D.J. Lipomi, Energy Environ. Sci. 8 (2015) 55-80.

[11] R. Sharma, A. Sharma, S. Agarwal, M.S. Dhaka, Sol. Energy 244 (2022) 516-535.

[12] S. Rijal, D.-B. Li, R.A. Awni, S.S. Bista, Z. Song, Y. Yan, ACS Appl. Energy Mater. 4

(2021) 4313-4318.

[13] R. Tang, S. Chen, Z.-H. Zheng, Z.-H. Su, J.-T. Luo, P. Fan, X.-H. Zhang, J. Tang, G.-X. Liang, Adv. Mater. 34 (2022) 2109078.

[14] X. Wen, C. Chen, S. Lu, K. Li, R. Kondrotas, Y. Zhao, W. Chen, L. Gao, C. Wang, J. Zhang, G. Niu, J. Tang, Nat. Commun. 9 (2018) 2179.

[15] Z. Zhang, M. Hu, T. Jia, J. Du, C. Chen, C. Wang, Z. Liu, T. Shi, J. Tang, Y. Leng, ACS Energy Lett. 6 (2021) 1740-1748.

[16] C. Chen, K. Li, F. Li, B. Wu, P. Jiang, H. Wu, S. Lu, G. Tu, Z. Liu, J. Tang, ACS Photonics 7 (2020) 352-360.

[17] Y. Zhou, L. Wang, S. Chen, S. Qin, X. Liu, J. Chen, D.-J. Xue, M. Luo, Y. Cao, Y. Cheng, E.H. Sargent, J. Tang, Nat. Photonics 9 (2015) 409-415.

[18] P. Fan, G.-J. Chen, S. Chen, Z.-H. Zheng, M. Azam, N. Ahmad, Z.-H. Su, G.-X. Liang, X.-H. Zhang, Z.-G. Chen, ACS Appl. Mater. Interfaces 13 (2021) 46671-46680.

[19] K. Li, F. Li, C. Chen, P. Jiang, S. Lu, S. Wang, Y. Lu, G. Tu, J. Guo, L. Shui, Z. Liu, B. Song, J. Tang, Nano Energy 86 (2021) 106101.

[20] G.-X. Liang, Y.-D. Luo, S. Chen, R. Tang, Z.-H. Zheng, X.-J. Li, X.-S. Liu, Y.-K. Liu, Y.-F. Li, X.-Y. Chen, Z.-H. Su, X.-H. Zhang, H.-L. Ma, P. Fan, Nano Energy 73 (2020) 104806.

[21] Z. Duan, X. Liang, Y. Feng, H. Ma, B. Liang, Y. Wang, S. Luo, S. Wang, R.E.I. Schropp, Y. Mai, Z. Li, Adv. Mater. 34 (2022) 2202969.

[22] X. Wen, Z. Lu, G.-C. Wang, M.A. Washington, T.-M. Lu, Nano Energy 85 (2021) 106019.

[23] X. Liang, Y. Feng, W. Dang, H. Huang, X. Wang, Y. Guo, K. Shen, R.E.I. Schropp, Z. Li, Y. Mai, ACS Energy Lett. 8 (2023) 213-221.

[24] X. Wen, Z. Lu, X. Yang, C. Chen, M.A. Washington, G.-C. Wang, J. Tang, Q. Zhao, T.-M. Lu, ACS Appl. Mater. Interfaces 15 (2023) 22251-22262.

[25] J. Liu, Q. Shen, Z. Liu, X. Gao, Z. Zhang, X. Liu, K. Cheng, Z. Du, ACS Appl. Mater. Interfaces 13 (2021) 31852-31860.

[26] J. Luo, W. Xiong, G. Liang, Y. Liu, H. Yang, Z. Zheng, X. Zhang, P. Fan, S. Chen, J. Alloys Compd. 826 (2020) 154235.

[27] G. Liang, M. Chen, M. Ishaq, X. Li, R. Tang, Z. Zheng, Z. Su, P. Fan, X. Zhang, S. Chen, Adv. Sci. 9 (2022) 2105142.

[28] Z. Li, X. Chen, H. Zhu, J. Chen, Y. Guo, C. Zhang, W. Zhang, X. Niu, Y. Mai, Sol. Energy Mater. Sol. Cells 161 (2017) 190-196.

[29] R. Tang, Z.-H. Zheng, Z.-H. Su, X.-J. Li, Y.-D. Wei, X.-H. Zhang, Y.-Q. Fu, J.-T. Luo, P. Fan, G.-X. Liang, Nano Energy 64 (2019) 103929.

[30] J. Lin, A. Mahmood, G. Chen, N. Ahmad, M. Chen, P. Fan, S. Chen, R. Tang, G. Liang, Mater. Today Phys. 27 (2022) 100772.

[31] J. Tao, X. Hu, J. Xue, Y. Wang, G. Weng, S. Chen, Z. Zhu, J. Chu, Sol. Energy Mater. Sol. Cells 197 (2019) 1-6.

[32] K. Li, S. Wang, C. Chen, R. Kondrotas, M. Hu, S. Lu, C. Wang, W. Chen, J. Tang, J. Mater. Chem. A 7 (2019) 9665-9672.

[33] Q. Cang, H. Guo, X. Jia, H. Ning, C. Ma, J. Zhang, N. Yuan, J. Ding, Sol. Energy 199 (2020) 19-25.

[34] Z. Li, X. Liang, G. Li, H. Liu, H. Zhang, J. Guo, J. Chen, K. Shen, X. San, W. Yu, R.E.I. Schropp, Y. Mai, Nat. Commun. 10 (2019) 125.

[35] S. Rijal, D.-B. Li, R.A. Awni, C. Xiao, S.S. Bista, M.K. Jamarkattel, M.J. Heben, C.-S. Jiang, M. Al-Jassim, Z. Song, Y. Yan, Adv. Funct. Mater. 32 (2022) 2110032.

[36] G. Lee, M.-c. Kim, Y.W. Choi, N. Ahn, J. Jang, J. Yoon, S.M. Kim, J.-G. Lee, D. Kang, H.S. Jung, M. Choi, Energy Environ. Sci. 12 (2019) 3182-3191.

[37] C. Peng, Z. Jia, H. Neilson, T. Li, J. Lou, Adv. Energy Mater. 15 (2013) 250-256.

[38] X.-Y. Chen, M. Ishaq, N. Ahmad, R. Tang, Z.-H. Zheng, J.-G. Hu, Z.-H. Su, P. Fan, G.-X. Liang, S. Chen, J. Mater. Chem. A 10 (2022) 22791-22802.

[39] C. Chen, D.C. Bobela, Y. Yang, S. Lu, K. Zeng, C. Ge, B. Yang, L. Gao, Y. Zhao, M.C. Beard, J. Tang, Frontiers of Optoelectronics 10 (2017) 18-30.

[40] K.C. Gödel, Y.C. Choi, B. Roose, A. Sadhanala, H.J. Snaith, S.I. Seok, U. Steiner, S.K. Pathak, Chem. Commun. 51 (2015) 8640-8643.

[41] C. Chen, J. Tang, ACS Energy Lett. 5 (2020) 2294-2304.

[42] C. Guo, X. Liang, T. Liu, Y. Liu, L. Yang, W. Lai, R.E.I. Schropp, D. Song, Y. Mai, Z. Li, Sol. RRL 4 (2020) 2000054.

[43] Y. Song, B. Yao, Y. Li, Z. Ding, R. Liu, Y. Sui, L. Zhang, Z. Zhang, H. Zhao, ACS Appl. Energy Mater. 2 (2019) 2230-2237.

[44] Y. Zhao, Z. Yu, J. Hu, Z. Zheng, H. Ma, K. Sun, X. Hao, G. Liang, P. Fan, X. Zhang, Z. Su, J. Energy Chem. 75 (2022) 321-329.

[45] R. Sakdanuphab, C. Chityuttakan, A. Pankiew, N. Somwang, K. Yoodee, S. J. Cryst. Growth 319 (2011) 44-48.

[46] K.-J. Yang, S. Kim, S.-Y. Kim, D.-H. Son, J. Lee, Y.-I. Kim, S.-J. Sung, D.-H. Kim, T. Enkhbat, J. Kim, J. Kim, W. Jo, J.-K. Kang, Adv. Funct. Mater. 31 (2021) 2102238.

[47] F. Sadegh, E. Akman, D. Prochowicz, M.M. Tavakoli, P. Yadav, S. Akin, ACS Appl. Mater. Interfaces 14 (2022) 38631-38641.

[48] O. Gunawan, T.K. Todorov, D.B. Mitzi, Appl. Phys. Lett. 97 (2010) 233506.

[49] B. Xu, X. Lu, C. Ma, Y. Liu, R. Qi, R. Huang, Y. Chen, P. Yang, J. Chu, L. Sun, IEEE J. Photovolt. 10 (2020) 1191-1200.

[50] G.S. Park, V.B. Chu, B.W. Kim, D.-W. Kim, H.-S. Oh, Y.J. Hwang, B.K. Min, ACS Appl. Mater. Interfaces 10 (2018) 9894-9899.

[51] Y.-D. Luo, R. Tang, S. Chen, J.-G. Hu, Y.-K. Liu, Y.-F. Li, X.-S. Liu, Z.-H. Zheng, Z.-H. Su, X.-F. Ma, P. Fan, X.-H. Zhang, H.-L. Ma, Z.-G. Chen, G.-X. Liang, Chem. Eng. J. 393 (2020) 124599.

[52] X. Hu, J. Tao, G. Weng, J. Jiang, S. Chen, Z. Zhu, J. Chu, Sol. Energy Mater. Sol. Cells 186 (2018) 324-329.

[53] J. Li, S. Kim, D. Nam, X. Liu, J. Kim, H. Cheong, W. Liu, H. Li, Y. Sun, Y. Zhang, Sol. Energy Mater. Sol. Cells 159 (2017) 447-455.

[54] H. Deng, Q. Sun, Z. Yang, W. Li, Q. Yan, C. Zhang, Q. Zheng, X. Wang, Y. Lai, S. Cheng, Nat. Commun. 12 (2021) 3107.

[55] J. Zheng, C. Liu, L. Zhang, Y. Chen, F. Bao, J. Liu, H. Zhu, K. Shen, Y. Mai, Chem. Eng. J. 446 (2022) 136474.

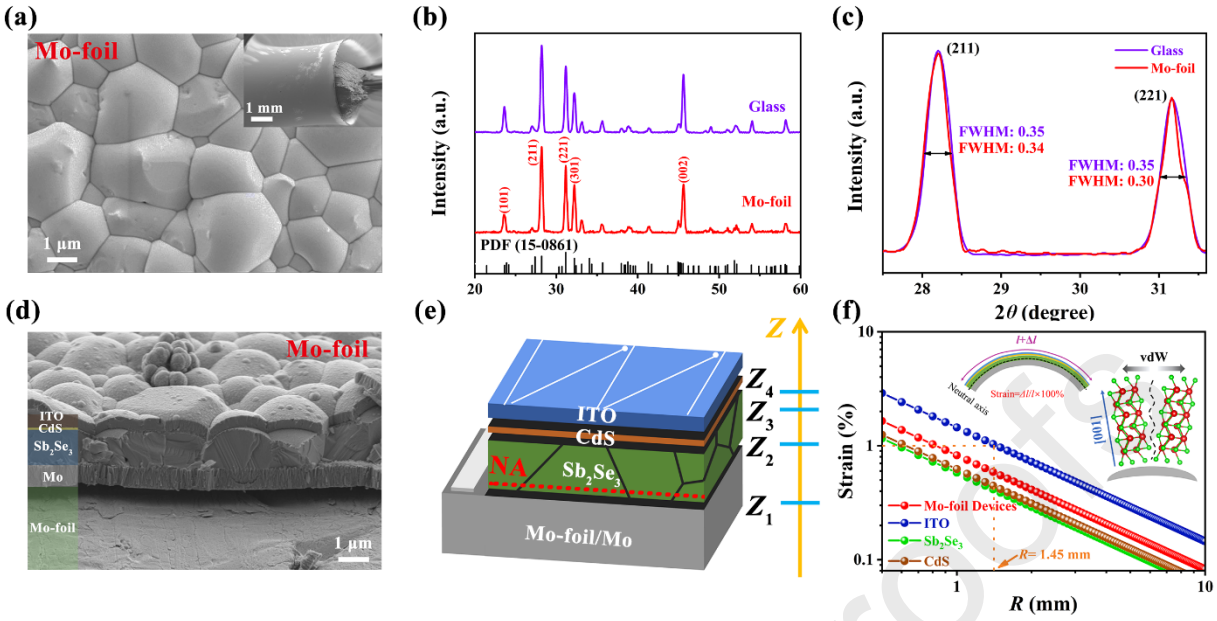


**Fig. 1.** (a) Top-view SEM images of the $Sb_2Se_3$ thin films deposited on flexible Mo-foil substrates. The $Sb_2Se_3$ thin films were bending at a 2 mm radius. The inset is the SEM image of the thin films at a 1 mm bar. (b) XRD patterns, and (c) the full width at half maximum (FWHM) of the representative (211) and (221) XRD diffraction peaks of the $Sb_2Se_3$ thin films on Mo-foil and Glass substrates. (d) Cross-sectional SEM image of the Mo-foil $Sb_2Se_3$ thin-film solar cell. (e) Schematic diagram of the neutral axis (NA) in flexible Mo-foil $Sb_2Se_3$ solar cell. $Z_k$ stands for the center position of each layer. NA of the whole device is marked by a red dash line. (f) The strain of the whole device, $Sb_2Se_3$, CdS and ITO layers as a function of radius. The inset in the upper right corner is the crystal structure of $Sb_2Se_3$, wherein, the black dash line marks the gap between $[Sb_4Se_6]_n$ ribbons.

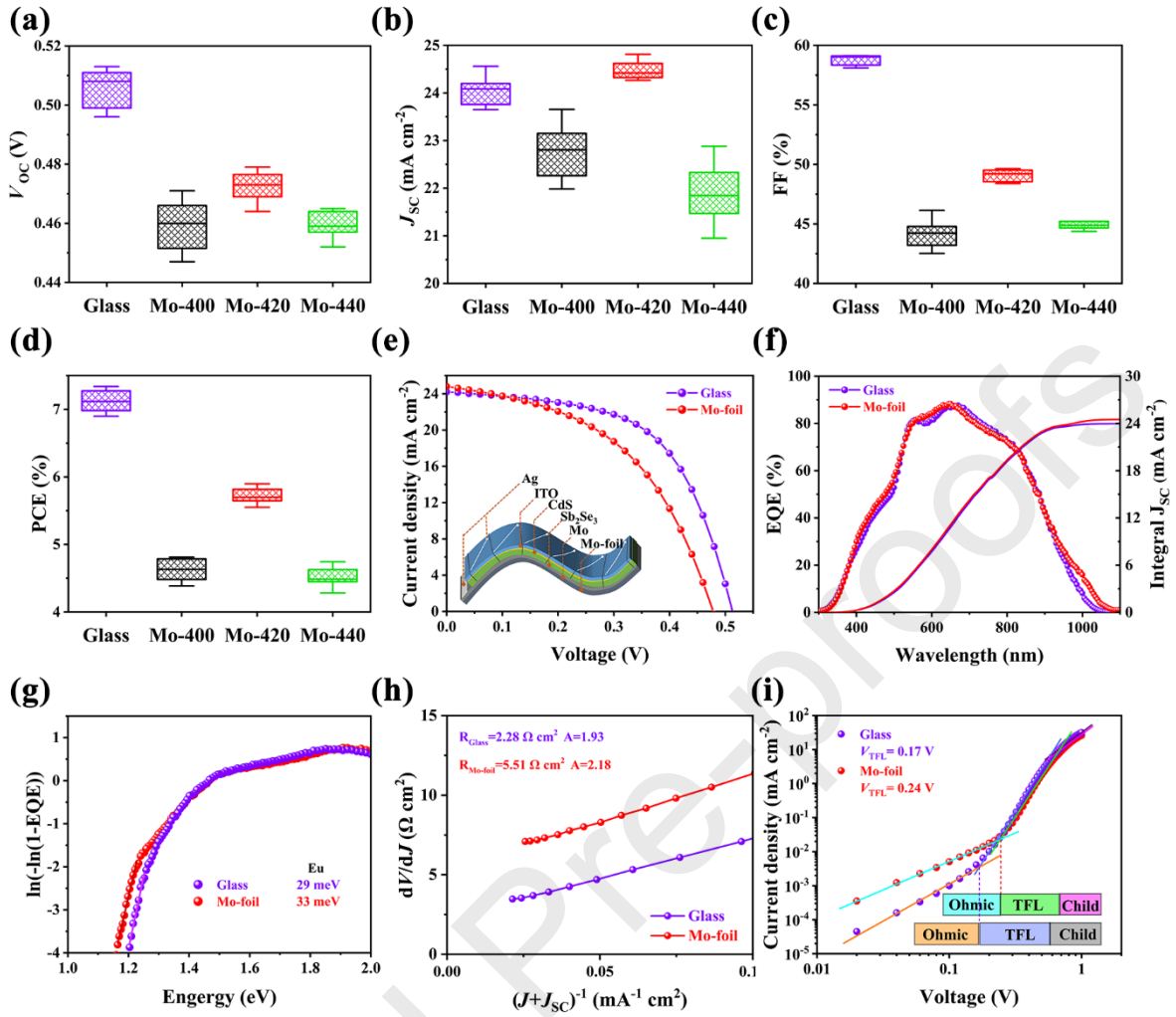


**Fig. 2.** Statistical distribution of the key performance parameters of the $Sb_2Se_3$ thin-film solar cells, including (a) $V_{OC}$, (b) $J_{SC}$, (c) FF, and (d) PCE. (e) *J-V* curves of the representative Glass and Mo-foil $Sb_2Se_3$ thin-film solar cells, and a schematic configuration of the flexible device (insert). (f) EQE and integrated $J_{SC}$ of the devices. (g) The Urbach energy ($E_u$) extracted from EQE. (h) Series resistance *R* and ideality factor *A* characterizations, (i) Logarithmic *J-V* curves, showing Ohmic, TFL, and Child region.

**Table 1.** Device performance parameters of $Sb_2Se_3$ thin-film solar cells with different substrate conditions.

| Devices | PCE (%) | $V_{OC}$ (V) | FF (%) | $J_{SC}$ (mA cm$^{-2}$) |
|---|---|---|---|---|
| Glass | 7.34 | 0.513 | 59.11 | 24.20 |
| Mo-foil W/O NaF | 5.90 | 0.479 | 49.63 | 24.81 |
| Mo-foil With NaF | 8.03 | 0.492 | 62.30 | 26.21 |

**Table 2.** A comparison of photovoltaic parameters with state-of-the-art flexible $Sb_2Se_3$ devices.

| Substrate | Device configuration | PCE (%) | $V_{OC}$ (V) | $J_{SC}$ (mA cm$^{-2}$) | FF (%) | Ref. |
|---|---|---|---|---|---|---|
| Mo-foil | Mo/$Sb_2Se_3$/$In_2S_3$/ZnO/ITO | 5.35 | 0.370 | 28.22 | 51.90 | [9] |
| PI | ITO/CdS/$Sb_2Se_3$/Au | 6.13 | 0.415 | 25.50 | 58.00 | [19] |
| Photoresist | ITO/CdS/$Sb_2Se_3$/Au | 7.15 | 0.426 | 29.30 | 57.30 | [22] |
| PI | Mo/PbSe/$Sb_2Se_3$/CdS/ZnO/AZO/Ag | 8.43 | 0.452 | 29.00 | 64.30 | [23] |
| Mica | Mo/$Sb_2Se_3$/CdS/ITO/Ag | 8.42 | 0.470 | 31.30 | 57.30 | [24] |
| Mo-foil | Mo/$Sb_2Se_3$/CdS/ITO/Ag | 5.90 | 0.479 | 24.81 | 49.63 | This work |
| Mo-foil | Mo/NaF/$Sb_2Se_3$/CdS/ITO/Ag | 8.03 | 0.492 | 26.21 | 62.30 | This work |

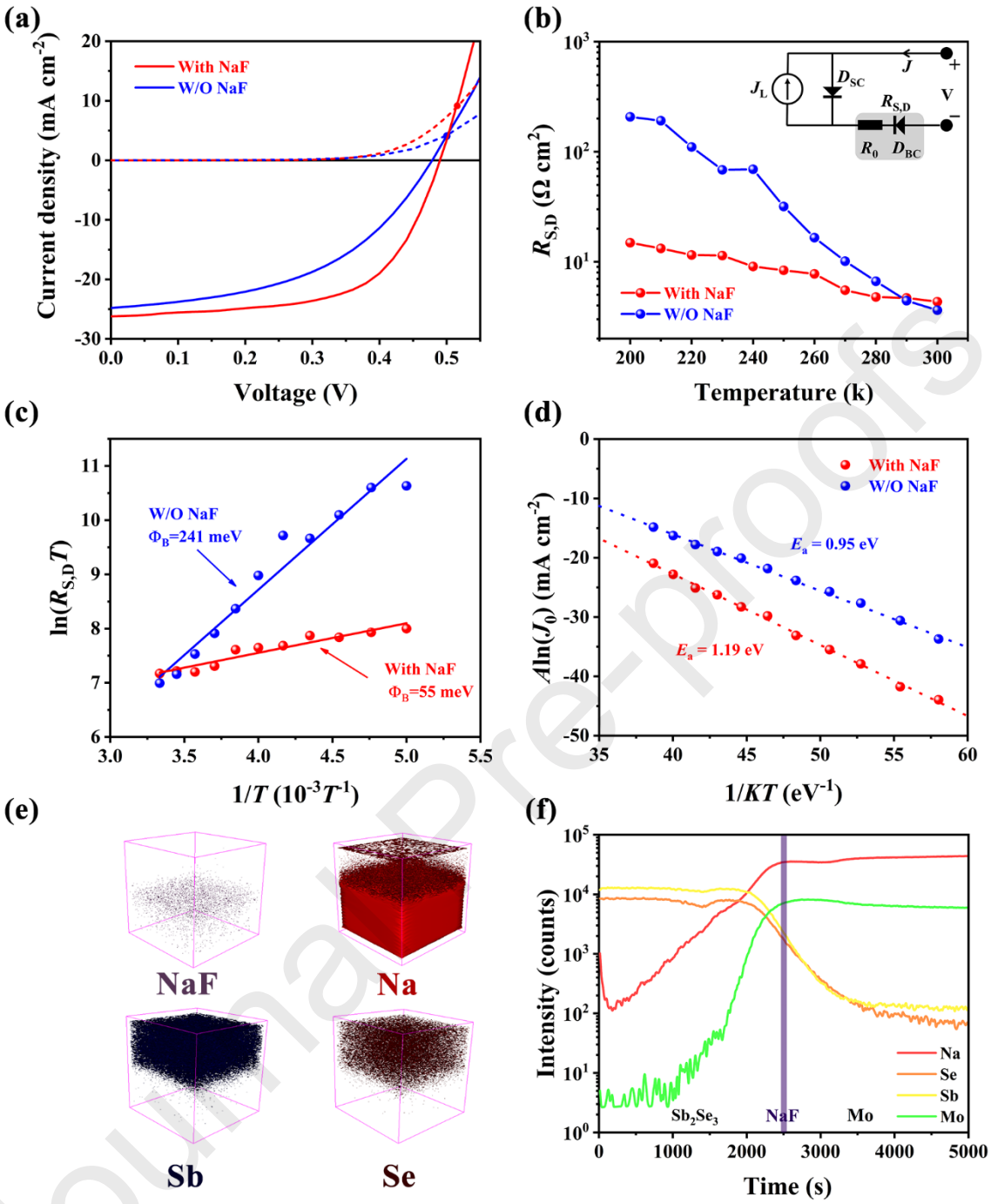


**Fig. 3.** (a) Light (solid line) and dark (dash line) *J-V* curves of the representative flexible Mo-foil $Sb_2Se_3$ devices with and without NaF (i.e., denoted as With NaF and W/O NaF). (b) Temperature-dependent $R_{S,D}$ of the devices, and a simple circuit model of the thin-film solar cell (insert). (c) Blocking contact barrier height determination of the devices. (d) $A\ln(J_0)$ versus $1/kT$ plots, wherein, $E_a$ values can be estimated from the slopes. (e) SIMS 3D images and (f) SIMS depth profiles, showing element distributions of the Mo/NaF/$Sb_2Se_3$ device.

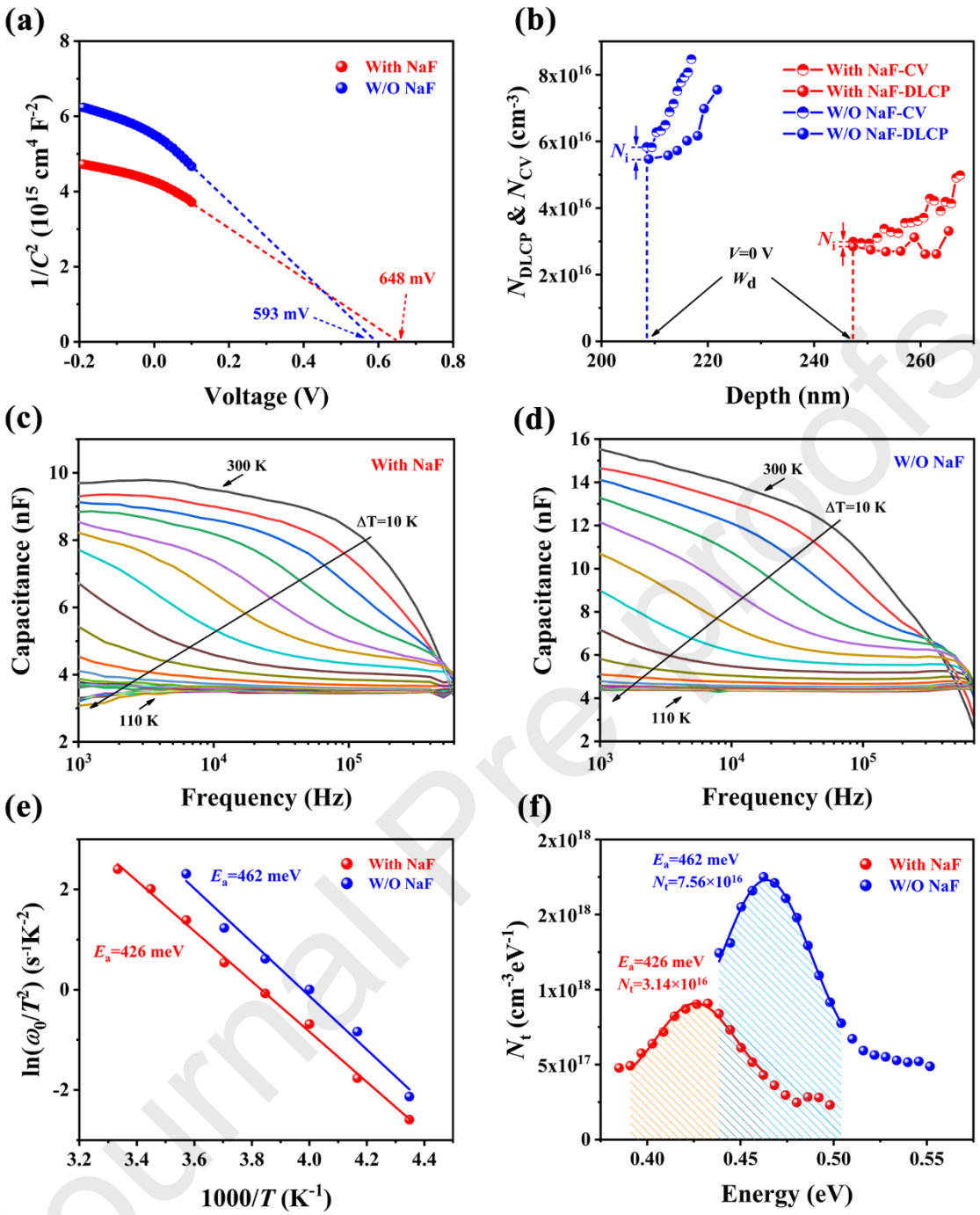


**Fig. 4.** (a) $1/C^2$-$V$ plots, and (b) $C$-$V$ and DLCP profiles of the Mo-foil $Sb_2Se_3$ devices With and W/O NaF interface layer. Admittance spectra of (c) With NaF and (d) W/O NaF Mo-foil $Sb_2Se_3$ devices. (e) Defect activation energies, and (f) defect density spectra of the corresponding devices.

**Table 3.** Summary of heterojunction and interface associated photovoltaic parameters of the $Sb_2Se_3$ devices.

| Devices | $E_u$ (meV) | A | $V_{TFL}$ (V) | $N_{trap}$ ($cm^{-3}$) | $\Phi_B$ (meV) | $E_a$ (eV) | $V_{bi}$ (V) | $N_i$ ($cm^{-3}$) |
|---|---|---|---|---|---|---|---|---|
| Glass | 29 | 1.93 | 0.17 | $1.26\times10^{14}$ | – | – | – | – |
| Mo-foil W/O NaF | 33 | 2.18 | 0.24 | $1.77\times10^{14}$ | 241 | 0.95 | 0.593 | $3.63\times10^{15}$ |
| Mo-foil With NaF | – | 1.62 | – | – | 55 | 1.19 | 0.648 | $1.45\times10^{15}$ |

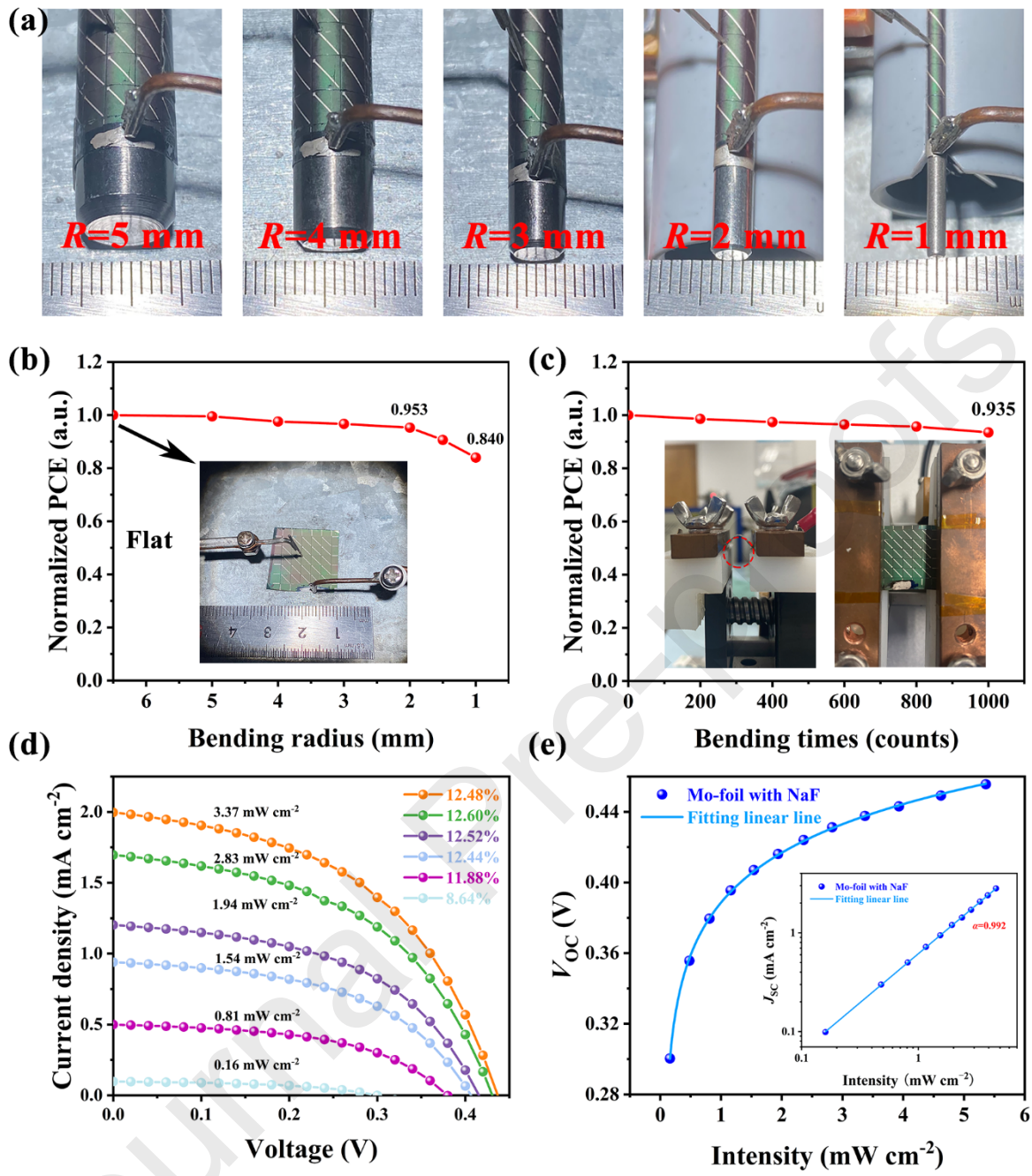


**Fig. 5.** (a) Photographs of flexible Mo-foil $Sb_2Se_3$ solar cells at different bending radii. (b) Normalized PCE degradation at different bending *R* (Flat to 1 mm). Inset: photograph of the flexible device in its initial planar state. (c) Normalized PCE evolution with different bending cycles (0–1000 times) at a 3 mm *R*. Inset: the schematic diagram of the bending equipment and the bending state of the device. (d) *J-V* curves of the flexible Mo-foil $Sb_2Se_3$ devices measured at low illumination intensities. (e) The device $V_{OC}$ and $J_{SC}$ evolution upon LED light intensity.

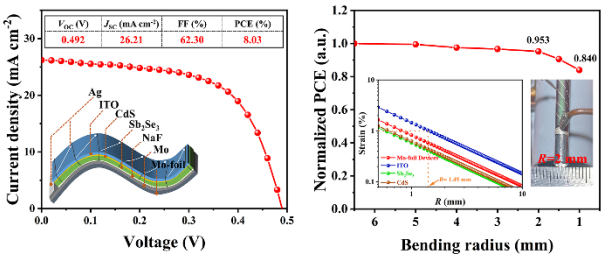


**Graphic abstract**

NaF intermediate is introduced to simultaneously optimize back contact and passivate detrimental defects. Over 8% efficient flexible $Sb_2Se_3$ thin-film solar cell can be achieved, accompanied with superior flexibility and weak light photo-response.

# Supporting Information

## Interface optimization and defects suppression via NaF introduction enable efficient flexible $Sb_2Se_3$ thin-film solar cells

*Mingdong Chen[a,c], Muhammad Ishaq[a], Donglou Ren[b], Hongli Ma[c], Zhenghua Su[a], Ping Fan[a], David Le Coq[c], Xianghua Zhang[c], Guangxing Liang[a], Shuo Chen[a,]**

[a]Shenzhen Key Laboratory of Advanced Thin Films and Applications, Key Laboratory of Optoelectronic Devices and Systems of Ministry of Education and Guangdong Province, College of Physics and Optoelectronic Engineering, Shenzhen University, Shenzhen, 518060, Guangdong, China

[b]State Key Laboratory of Featured Metal Materials and Life-cycle Safety for Composite Structures, MOE Key Laboratory of New Processing Technology for Nonferrous Metals and Materials, School of Resources, Environment and Materials, Guangxi University, Nanning, 530004, Guangxi, China

[c]CNRS, ISCR (Institut des Sciences Chimiques de Rennes), UMR 6226, Université de Rennes, Rennes, F-35000, France

[*]Corresponding author.

*E-mail address*: chensh@szu.edu.cn (S. Chen)

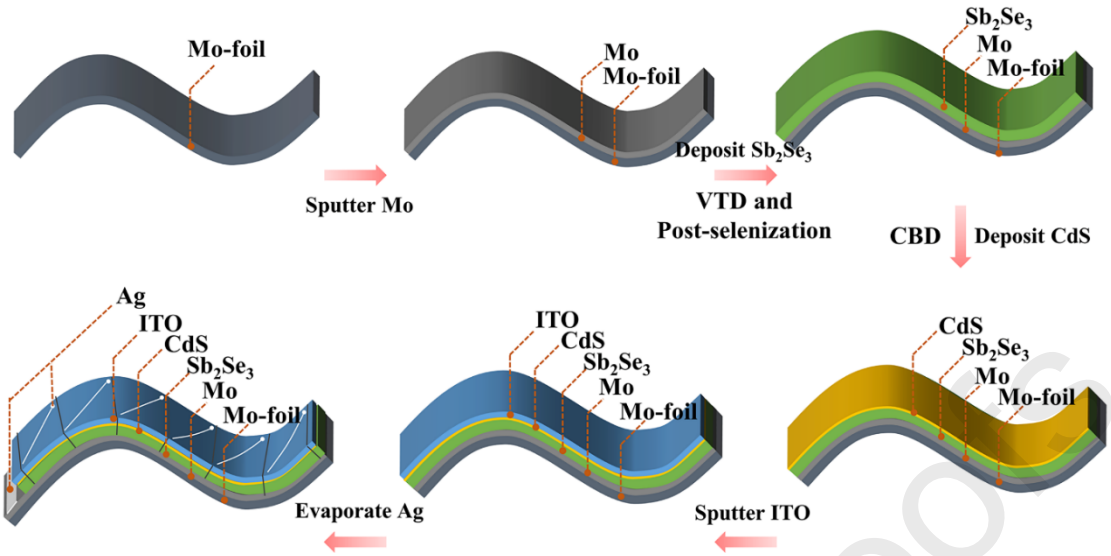


**Fig. S1.** Schematic illustration of the preparation process of the flexible Mo-foil substrate structured $Sb_2Se_3$ thin-film solar cells.

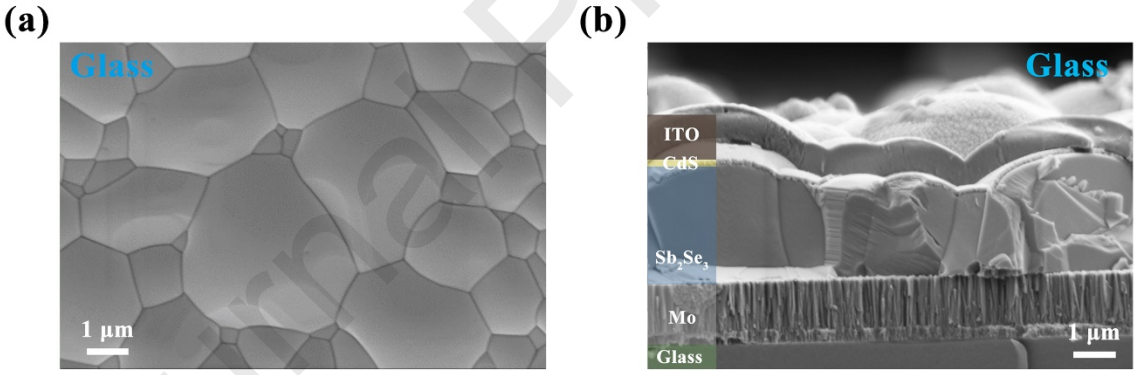


**Fig. S2.** (a) SEM top-view image of the $Sb_2Se_3$ thin film deposited on glass substrates, labeled as Glass $Sb_2Se_3$. (b) Cross-sectional SEM image of the Glass $Sb_2Se_3$ thin-film solar cell.

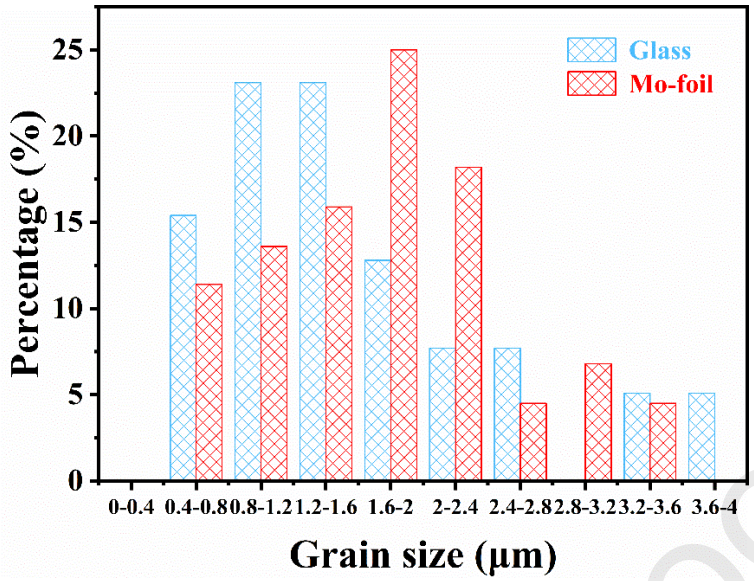


**Fig. S3.** The crystal size distribution diagram of $Sb_2Se_3$ thin films. The average grain size is 1.73 μm and 1.63 μm for Glass and Mo-foil $Sb_2Se_3$, respectively.

**Table S1.** The thickness, Young modulus and Poisson ratio of each layers.

| Layer | Thickness (μm) | Young modulus (Gpa) | Poisson ratio |
|---|---|---|---|
| Mo-foil | 30 | 329 | 0.31 |
| Mo | 0.7 | 329 | 0.31 |
| $Sb_2Se_3$ | 1.2 | 83 | 0.26 |
| CdS | 0.07 | 68 | 0.34 |
| ITO | 0.4 | 135 | 0.27 |

**Supplementary note 1. The strain analysis of $Sb_2Se_3$ layer, ITO layer and device**

The neutral axis (NA) is the key factor to estimate the strain of device under bending states. The locations of NA ($z_{NA}$) is determined by the total force in the cross section, where the strain in the film is zero. The relationship between $z_{NA}$ and strain under different curvature radii (R) is shown in the following equation [1–3].

$$z_{NA} = \frac{\sum_{k=1}^{n} E_k^* t_k^* z_k}{\sum_{k=1}^{n} E_k^* t_k^*} \quad \text{(S1)}$$

$$E_k^* = \frac{E_k}{1-\nu_k^2} \quad \text{(S2)}$$

$$\varepsilon(z,R) = \frac{z - z_{NA}}{R} \quad \text{(S3)}$$

Where $E_k$, $\nu_k$ and $t_k$ are Young's modulus, Poisson's ratio and thickness of each layer, respectively, and $z_k$ is the coordinate of half thickness film. Then we can obtain the R dependent strain ($\varepsilon_z$). All calculation parameters are listed in Table S1.

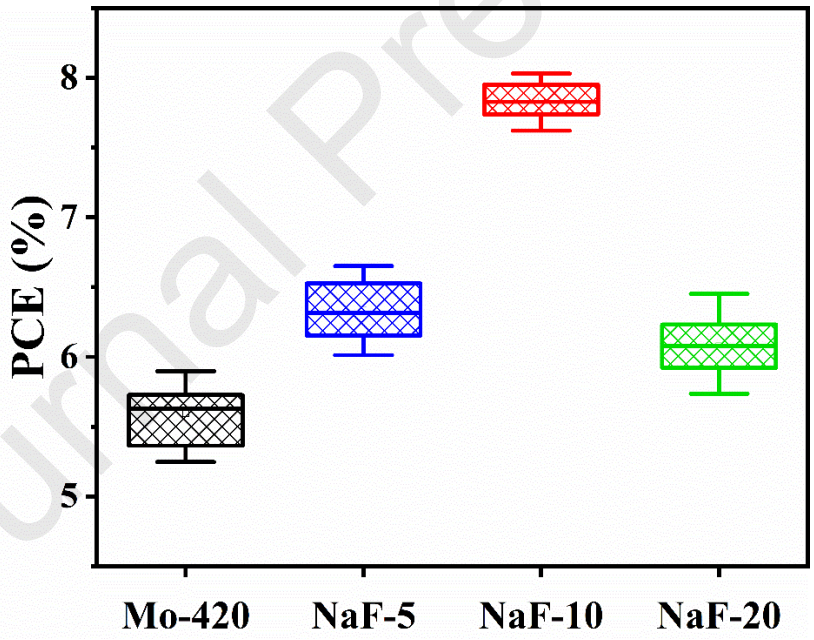


**Fig. S4.** The statistical PCE distribution boxplots of the flexible $Sb_2Se_3$ thin-film solar cells with different NaF interface layer thicknesses.

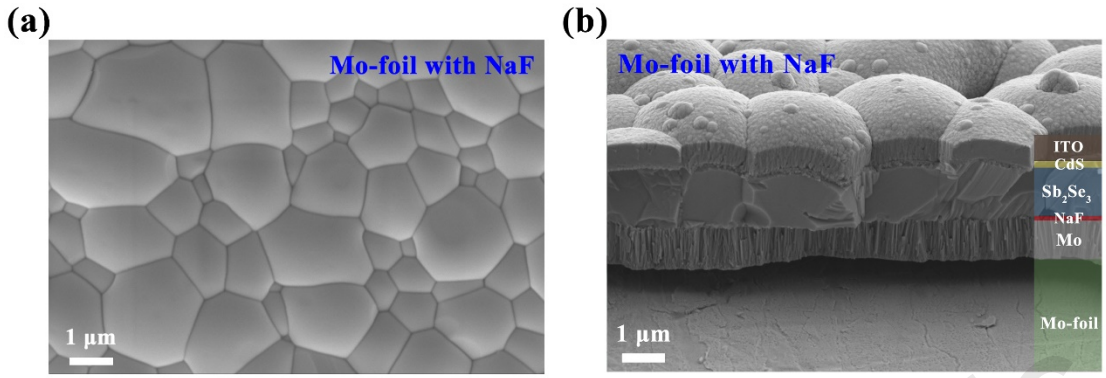


**Fig. S5.** (a) SEM top-view images of the flexible $Sb_2Se_3$ thin films with NaF interface layer introduction. (b) Cross-sectional SEM image of the flexible $Sb_2Se_3$ thin -film solar cell with NaF.

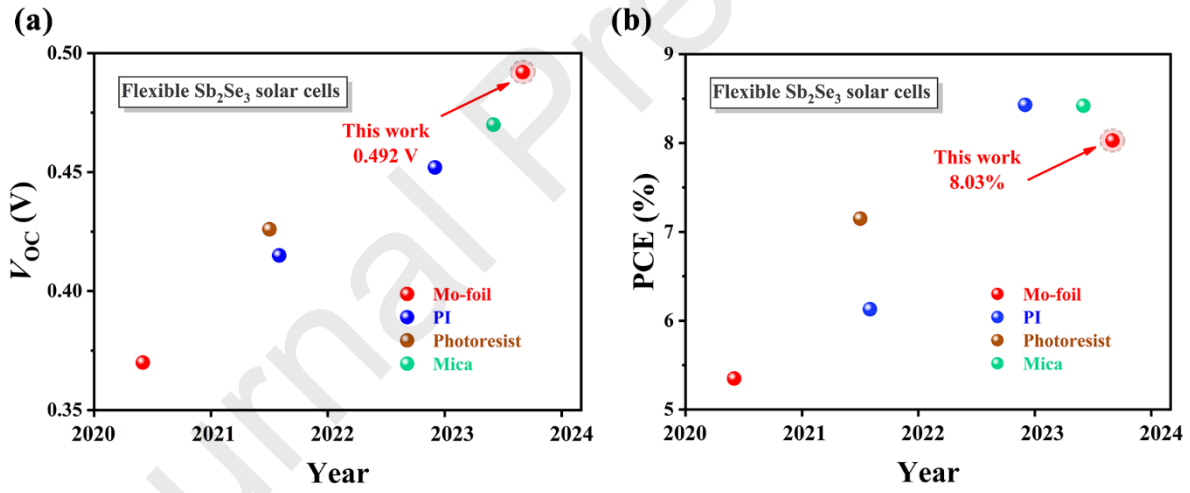


**Fig. S6.** (a) $V_{OC}$, and (b) PCE statistics of the flexible $Sb_2Se_3$ solar cells prepared based on different substrates [3–7].

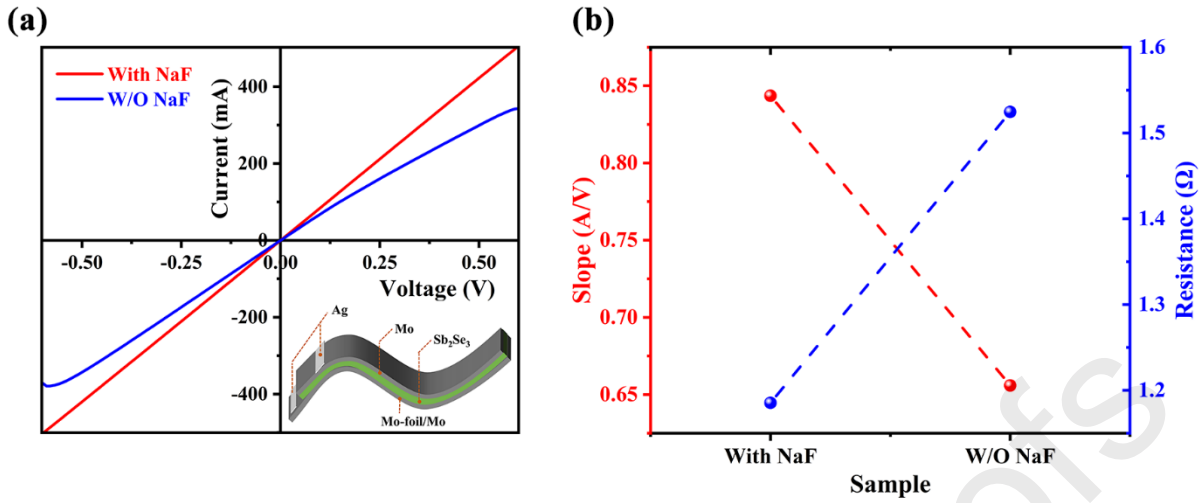


**Fig. S7.** (a) *I-V* curves of the flexible Mo-foil/Mo/$Sb_2Se_3$ back contact with NaF layer and without NaF layer (the schematic diagram of device structure used to test *I-V* curves was inserted). (b) The slopes and resistance curves of With NaF and W/O NaF samples.

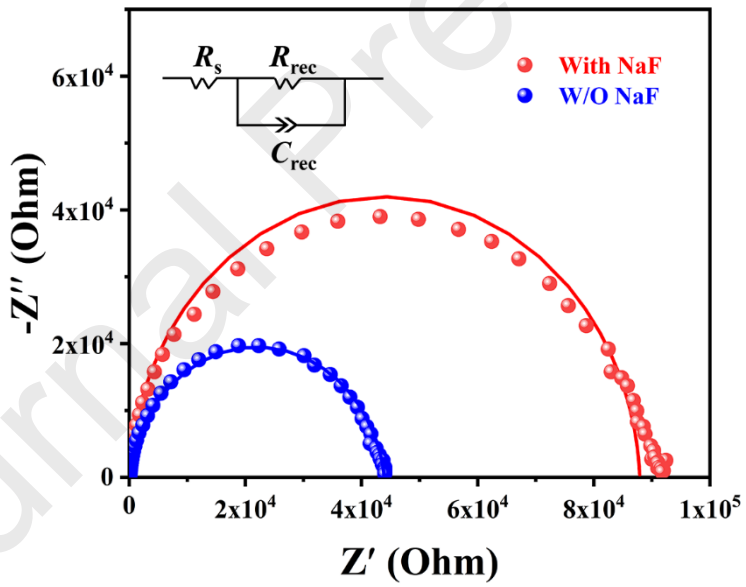


**Fig. S8.** Electrochemical recombination analysis in the devices. Nyquist plots of With NaF and W/O NaF devices. The inset shows the equivalent circuit diagram.

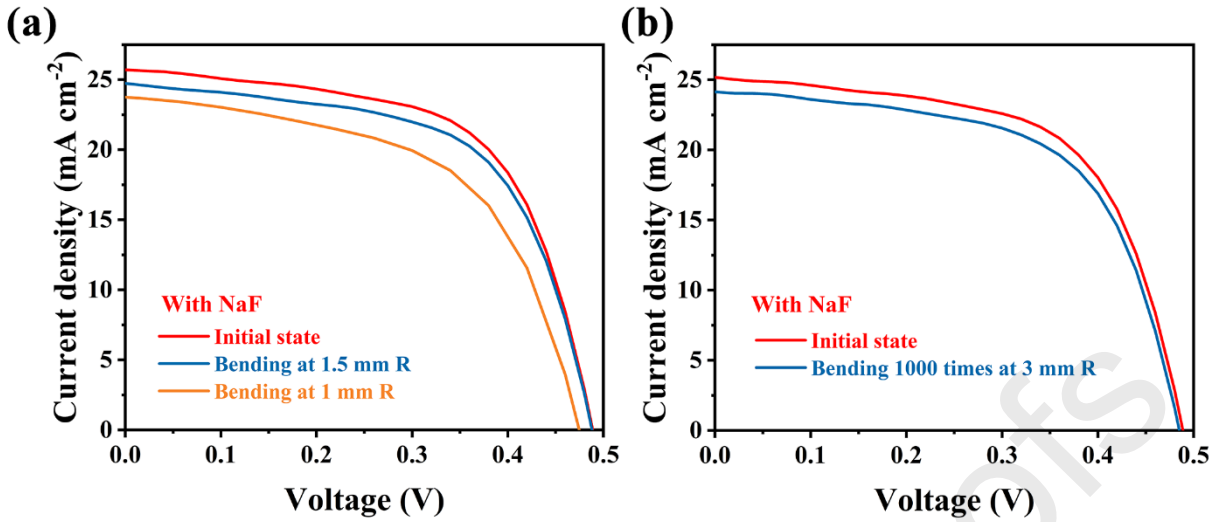


**Fig. S9.** (a) *J-V* curves of the flexible $Sb_2Se_3$ solar cells at initial state, and bending at a 1.5 mm and 1mm R. (b) *J-V* curves of the flexible $Sb_2Se_3$ solar cells at initial state and after bending at 3 mm R for 1000 times.

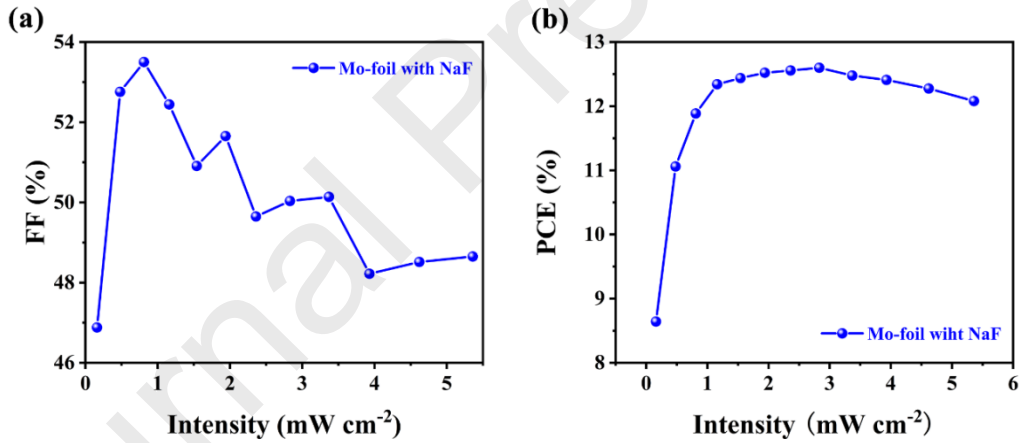


**Fig. S10.** (a) FF and (b) PCE evolution with the LED light intensity for flexible Mo-foil $Sb_2Se_3$ device.

**Table S2.** The performance parameters of the flexible $Sb_2Se_3$ solar cell bending at different R. The light intensity was calibrated by a standard Si-reference solar cell.

| Bending radius (mm) | $V_{OC}$ (V) | $J_{SC}$ (mA cm$^{-2}$) | FF (%) | PCE (%) |
|---|---|---|---|---|
| Flat | 0.491 | 25.70 | 61.90 | 7.80 |
| 5 | 0.491 | 25.54 | 61.86 | 7.76 |

| | | | | |
|---|---|---|---|---|
| 4 | 0.491 | 25.06 | 61.85 | 7.61 |
| 3 | 0.490 | 24.95 | 61.66 | 7.54 |
| 2 | 0.489 | 24.76 | 61.40 | 7.43 |
| 1.5 | 0.481 | 24.62 | 59.72 | 7.07 |
| 1 | 0.477 | 23.72 | 57.89 | 6.55 |

**Table S3.** The performance parameters of the flexible $Sb_2Se_3$ solar cells after different bending cycles.

| **Bending circles** | $V_{OC}$ **(V)** | $J_{SC}$ **(mA cm$^{-2}$)** | **FF (%)** | **PCE (%)** |
|---|---|---|---|---|
| 0 | 0.490 | 25.18 | 62.05 | 7.66 |
| 200 | 0.489 | 25.10 | 61.53 | 7.55 |
| 400 | 0.488 | 24.88 | 61.48 | 7.46 |
| 600 | 0.488 | 24.77 | 61.09 | 7.39 |
| 800 | 0.488 | 24.63 | 61.02 | 7.33 |
| 1000 | 0.486 | 24.14 | 61.00 | 7.16 |

**References**

[1] G. Lee, M.-c. Kim, Y.W. Choi, N. Ahn, J. Jang, J. Yoon, S.M. Kim, J.-G. Lee, D. Kang, H.S. Jung, M. Choi, Energy Environ. Sci. 12 (2019) 3182-3191.

[2] C. Chen, K. Li, F. Li, B. Wu, P. Jiang, H. Wu, S. Lu, G. Tu, Z. Liu, J. Tang, ACS Photonics 7 (2020) 352-360.

[3] K. Li, F. Li, C. Chen, P. Jiang, S. Lu, S. Wang, Y. Lu, G. Tu, J. Guo, L. Shui, Z. Liu, B. Song, J. Tang, Nano Energy 86 (2021) 106101.

[4] C. Wang, S. Lu, S. Li, S. Wang, X. Lin, J. Zhang, R. Kondrotas, K. Li, C. Chen, J. Tang,

Nano Energy 71 (2020) 104577.

[5] X. Wen, Z. Lu, G.-C. Wang, M.A. Washington, T.-M. Lu, Nano Energy 85 (2021) 106019.

[6] X. Liang, Y. Feng, W. Dang, H. Huang, X. Wang, Y. Guo, K. Shen, R.E.I. Schropp, Z. Li, Y. Mai, ACS Energy Lett. 8 (2023) 213-221.

[7] X. Wen, Z. Lu, X. Yang, C. Chen, M.A. Washington, G.-C. Wang, J. Tang, Q. Zhao, T.-M. Lu, ACS Appl. Mater. Interfaces 15 (2023) 22251-22262.

**Declaration of interests**

☒ The authors declare that they have no known competing financial interests or personal relationships that could have appeared to influence the work reported in this paper.

☐The authors declare the following financial interests/personal relationships which may be considered as potential competing interests: